

Article

Mechanism of Capacity Fading in the $\text{LiNi}_{0.8}\text{Co}_{0.1}\text{Mn}_{0.1}\text{O}_2$ Cathode Material for Lithium-Ion Batteries

Yong-keon Ahn ^{1,†}, Yong Nam Jo ^{2,†}, Woosuk Cho ², Ji-Sang Yu ² and Ki Jae Kim ^{1,*}

¹ Department of Energy Engineering, Konkuk University, 120 Neungdong-ro, Gwangjin-gu, Seoul 05029, Korea; sansojuice@naver.com

² Advanced Batteries Research Center, Korea Electronics Technology Institute, 25, Saenari-ro, Bundang-gu, Seongnam, Gyeonggi-do 13509, Korea; jyn@keti.re.kr (Y.N.J.); cho4153@keti.re.kr (W.C.); jisang@keti.re.kr (J.-S.Y.)

* Correspondence: kijaekim@konkuk.ac.kr

† These authors contributed equally to this work.

Received: 29 March 2019; Accepted: 26 April 2019; Published: 29 April 2019



Abstract: Understanding the capacity fading mechanism of the $\text{LiNi}_{0.8}\text{Co}_{0.1}\text{Mn}_{0.1}\text{O}_2$ (NCM811) cathode materials is crucial for achieving long-lasting lithium-ion batteries with high energy densities. In this study, we investigated the factors affecting the capacity fading of NCM811 during repeated cycling at high temperatures. We found that the change in the c-axis length during charging and discharging is the main cause of the formation and propagation of microcracks in the primary particles of NCM811. In addition, the electrolyte is decomposed on the microcrack surfaces and, consequently, by-products are formed on the particle surface, increasing the impedance and resulting in poor electronic and ionic connectivity between the primary particles of NCM811. In addition, the transition metals in the NCM811 cathode material are dissolved in the electrolyte from the newly formed microcrack surface between primary particles. Therefore, the electrolyte decomposition and transition metal dissolution on the newly formed surface are the major deteriorative effects behind the capacity fading in NCM811.

Keywords: microcrack; structural stability; capacity fading; NCM811; Ni-rich cathode material

1. Introduction

Thanks to growing concerns about global climate change, the development of environmentally sustainable energy technology is necessary [1–5]. The utilization of smart-grid systems and long-range electric vehicles (EVs), for instance, has become popular with regard to their efficient energy consumption; thus, the need for large-scale energy storage systems for electricity provision and control has increased significantly [6–9]. To meet these demands, batteries with high energy and power densities are a crucial prerequisite. Lithium-ion batteries (LIBs) are considered the most promising candidates owing to their high capacities, low self-discharging rates, and high operating potentials compared with other electrochemical energy storage devices [10–12].

To improve the energy density of LIBs, many researchers have focused on the development of cathode materials with high capacities, because the capacity limitation is related to the cathode in most LIB systems. Among the many cathode materials, nickel rich $\text{LiNi}_x\text{Co}_y\text{Mn}_z\text{O}_2$ (NCM, where $x + y + z = 1$, $x \geq 0.8$) has been spotlighted as one of the most feasible candidates for next-generation LIBs because of its high discharge capacity ($\sim 200 \text{ mAh g}^{-1}$), low cost, and low toxicity [13,14]. Although increasing the Ni content in NCM increases the specific discharge capacity, Ni-rich NCM shows significant performance degradation, which is mostly attributed to cation mixing, surface side reactions,

and intrinsic structural instability originating from the large volume changes during repeated cycling. Many solutions to overcome the poor cycle performance have been proposed, including surface coating, morphology control, and elemental doping [15–20]. Although cation mixing and surface side reactions can be inhibited by employing the above-mentioned solutions, the microcracks formed between primary particles, which is one of the main reasons for the poor cycle properties during repeated cycles at high temperature, remain problematic [21–25]. Many studies related to the effects of microcracks on the electrochemical performance of $\text{LiNi}_{0.85}\text{Co}_{0.1}\text{Al}_{0.05}\text{O}_2$ (lithium nickel cobalt aluminum oxide, NCA) or NCM have been reported, but the deteriorative effect of the microcracks on the electrochemical performance of Ni-rich NCM has not been adequately addressed. Therefore, understanding the negative effects of the microcracks is crucial to improving the cycling performance of Ni-rich NCM cathode materials.

Thus, we have focused on how the formation of microcracks between the primary particles affects the capacity fading of NCM811 during repeated charge cycling at high temperatures [26,27]. To understand the deteriorative effect of the microcracks in the secondary particles, a pouch-type full cell employing Ni-rich NCM cathode materials was prepared, and this cell was galvanostatically charged and discharged for 600 cycles at 45 °C. After 600 cycles, the pouch-type full cell was disassembled, and the structurally unstable Ni-rich NCM cathode materials were thoroughly analyzed. Finally, based on the experimental findings, the negative effects of the microcracks in the secondary particles on the electrochemical performance were identified.

2. Materials and Methods

Materials NCM811 (L&F, Korea) were used as the cathode material without further treatment. The shape and surface morphology of the NCM811 particles were examined using focused ion beam environmental scanning electron microscopy (FIB-ESEM, Quanta 3D FEG, FEI), and X-ray diffraction (XRD, Empyrean, PANalytical) was used for structural analysis. The cross-sectional specimens for transmission electron microscopy (TEM) measurements were prepared by ion milling (Ion slicer, JEOL, EM-09100 IS). The specimens were prepared by epoxy embedding, followed by mechanical milling, and ion milling. TEM (ARM-200F, JEOL) measurements, with a probe Cs aberration corrector (CEOS GmbH) and energy dispersive spectroscopy (EDS, X-MaxN80TLE, Oxford), were conducted to analyze the formation of microcracks in the NCM811 particles after cycling.

The electrochemical properties of NCM811 were tested in a pouch-type full cell and a coin-half cell. The cathode was prepared by casting slurries containing the active material (92 wt%), a conductive agent (Super P, 4 wt%), and a binder (polyvinylidene difluoride (PVdF), 4 wt%) in N-methylpyrrolidone (NMP) on an Al foil (15 μm) for both the pouch full cell and coin-half cell. The residual NMP was removed by drying under vacuum for 12 h at 120 °C. A natural graphite anode and a porous polyethylene membrane were used for full cell fabrication and a lithium metal was used as an anode for the coin-half cell. In addition, 1.0 M LiPF_6 dissolved in ethylene carbonate (EC)/ethyl methyl carbonate (EMC) (1:2 vol., PANAX Etec Co., Ltd., Nonsan, Korea) containing 3 wt% vinylene carbonate (VC) was used as the electrolyte for both the full cell and the coin-half cell. The cyclability of the full cell was tested in a voltage range from 3.0 to 4.2 V under a constant current at 1 C rate and 45 °C, and the coin cell was galvanostatically charged and discharged in a voltage range from 3.0 to 4.3 V (vs. Li/Li^+) to measure the reversible capacity and coulombic efficiency.

3. Results and Discussion

Before the high-temperature cycling tests, the morphology of the NCM811 cathode material was examined using FIB-ESEM. On the basis of the FIB-ESEM images (Figure 1a), the bare NCM811 particles have a typical spherical shape with an average size of 7 μm (Figure 1a inset) and were formed by the agglomeration of primary particles with a size of approximately 500 nm. To investigate the structure of the pristine NCM811, XRD measurements were performed, and the results are shown in Figure 1b. We observed noticeably separated (006)/(102) and (108)/(110) peaks, which are consistent

with the typical patterns of an ordered layered structure. Consequently, the pristine NCM811 cathode materials have the typical α -NaFeO₂ layered structure without any structural deformation or defects with a hexagonal crystal structure in the $R\text{-}3m$ space group, as illustrated in the schematic of the NCM811 crystal structure [28–32].

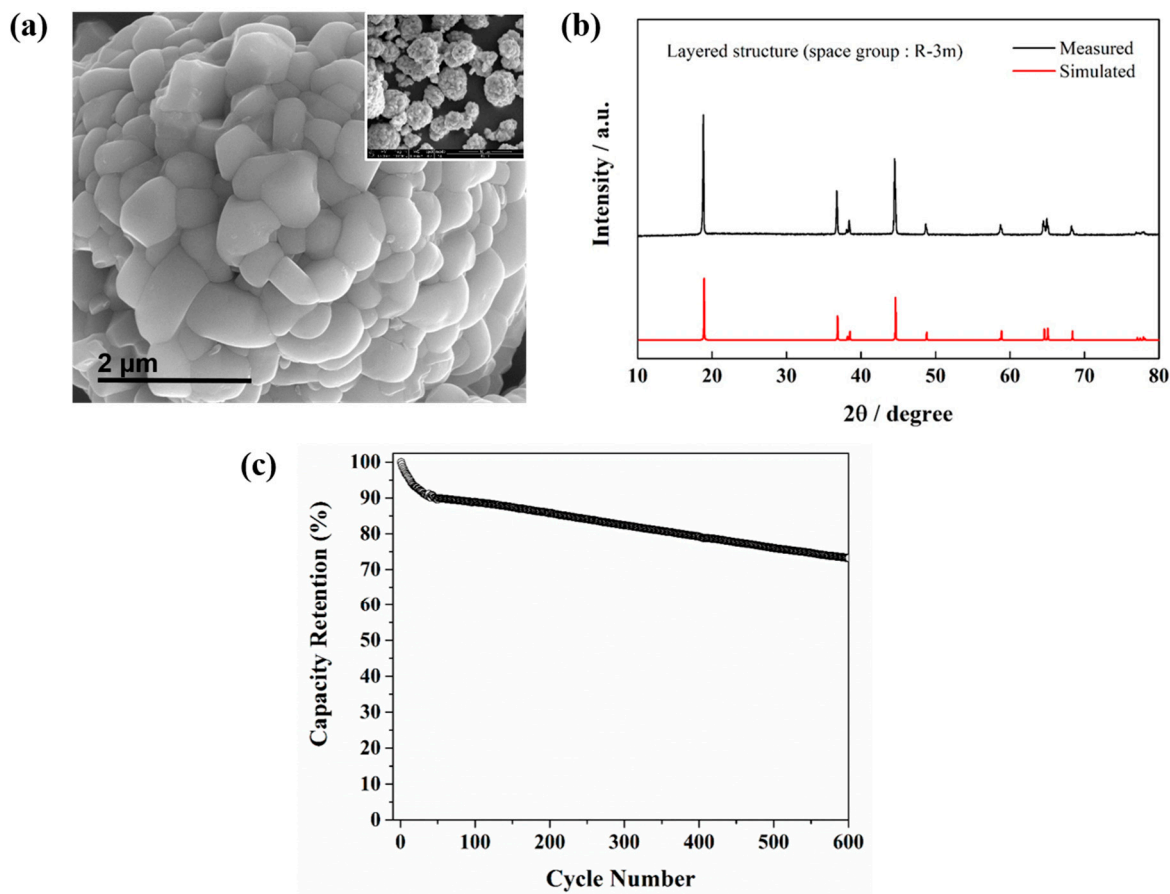


Figure 1. The morphology, structural, and electrochemical characteristics of the $\text{LiNi}_{0.8}\text{Co}_{0.1}\text{Mn}_{0.1}\text{O}_2$ (NCM811) cathode material. (a) Focused ion beam environmental scanning electron microscopy (FIB-ESEM) image of NCM811 secondary particles in which primary particles agglomerated into spheres. (b) X-ray diffraction (XRD) patterns indicating that NCM811 has a layered structure in the $R\text{-}3m$ space group. (c) Electrochemical performance over 600 cycles at 45 °C tested in a pouch-type full cell.

To understand the effect of the microcracks formed between primary particles on the capacity fading of the NCM811 cathode material during high-temperature cycling tests, a pouch-type full cell containing the NCM811 cathode material was prepared and galvanostatically charged and discharged for 600 cycles at 45 °C. As expected, the pouch-type full cell employing NCM811 showed poor cycle performance with a capacity retention of 73.2% of the initial discharge capacity after 600 galvanostatic cycles at 45 °C (Figure 1c). To understand the poor cycle life of NCM811, the pouch-type full cell was disassembled after 600 cycles, and the cycled NCM811 was analyzed by scanning transmission electron microscopy (STEM). Figure 2a shows a TEM image of cross-sectioned sample of NCM811 before cycling tests at 45 °C. Clearly, the primary particles are densely packed, and there are grain boundaries between the primary particles. In addition, there are no defects and microcracks. On the other hand, many cracks are formed and have propagated along the grain boundaries between the primary particles of the NCM811 cathode material particles after 600 cycles at 45 °C, as shown in Figure 2b, resulting in the poor cycle performance of NCM811.

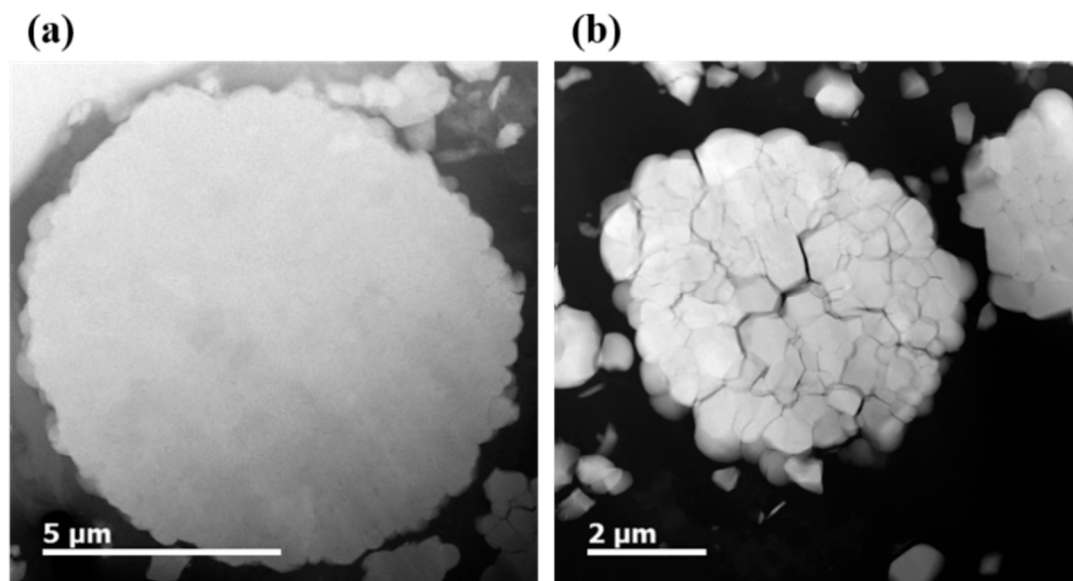


Figure 2. Cross-sectional scanning transmission electron microscopy (STEM) images for NCM811 (a) before cycling (bare) and (b) after 600 cycles at 45 °C.

To clarify the main cause of the microcracks between the primary particles of NCM811, in situ XRD observation was conducted with different cut-off voltages in the charge process. Figure 3a summarizes the changes in the c -axis with the degree of delithiation. The c -axis had its maximum value at around $x = 0.5$ and gradually decreased after $x > 0.5$. In particular, we found that the length of c -axis drastically decreased in the voltage range between 4.05 and 4.5 V versus Li/Li⁺. The change in the length of the c -axis seems to affect the formation of microcracks [33–37]. From the featured diffraction patterns of NCM811 in the charge process (Figure 3b), (003) reflection was adopted to ensure the structural variation in the Figure 3c. During Li⁺ desertion, peak shift tendency verifies the phase transition of NCM811 from hexagonal to monoclinic and then back to hexagonal, which was in good agreement with previous studies [38,39]. To confirm this, coin cells assembled with NCM811 were galvanostatically charged and discharged for 50 cycles under different charge cut-off voltages of 4.05, 4.30, and 4.50 V versus Li/Li⁺, respectively. The coin cells were disassembled after the cycling tests, and the cycled NCM811 cathode materials were analyzed by STEM (Figure 4). A small number of microcracks were observed on the NCM811 cathode materials that had been charged and discharged for 50 cycles at a cut-off voltage of 4.05 V, because the length of the c -axis is not significantly changed on the application of these charging cut-off voltages. On the other hand, many microcracks appeared on the NCM811 cathode materials that had been charged and discharged for 50 cycles at a cut-off voltage of 4.50 V, because the length of the c -axis was affected by these charging cut-off conditions. This result implies that the change in the length of the c -axis strongly affects the formation of microcracks in the NCM811 cathode materials. Consequently, we believe that the change in the c -axis during charging and discharging is one of the main causes of the formation of microcracks in the primary particles of NCM811 [22,25,33–35].

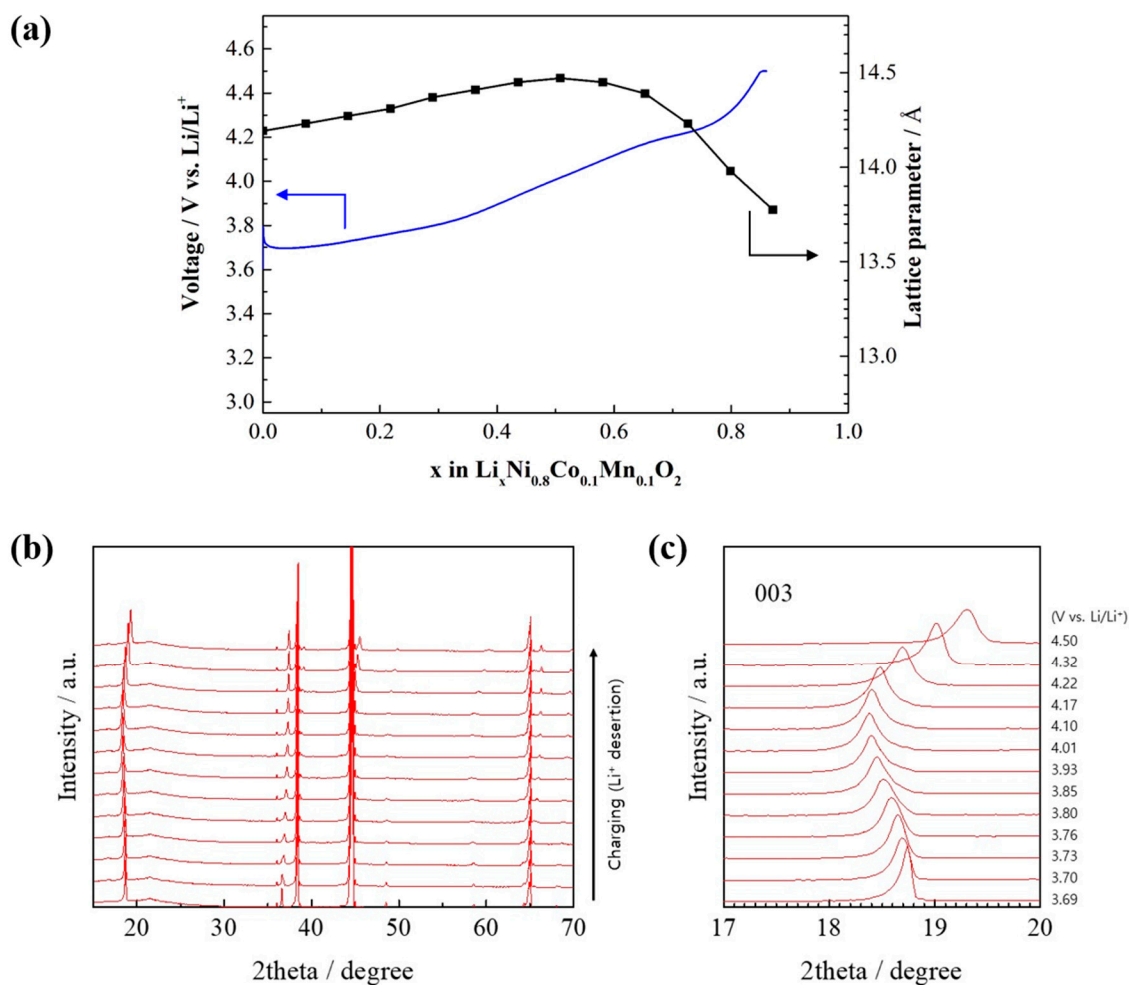


Figure 3. In situ XRD results of (a) the NCM811 crystal lattice variation during Li⁺ extraction (charged state), (b) diffraction patterns, and (c) 003 reflection.

To confirm the effects of the formation and propagation of microcracks on the capacity fading of NCM811 during repeated cycling, the chemical component of the surface microcracks was analyzed using EDS measurements for the cycled cathode. As displayed in Figure 5, fluorine was detected on the surface formed by the propagation of microcracks between the primary particles. The fluorine seems to originate from the decomposition of the lithium hexafluorophosphate (LiPF₆) salt in the liquid electrolyte that penetrated the newly formed microcracks between primary particles during repeated cycling, indicating that the new microcrack surface can promote the decomposition of the liquid electrolyte. It is well known that the by-products formed on the surface of cathode materials by the decomposition of the liquid electrolyte result in poor ionic and electronic connectivity in the primary particle subsurface [35,36]. Therefore, we believe that the by-products formed on the subsurface exposed by the propagation of the microcracks between primary particles would give rise to increased impedance and poor electronic and ionic connectivity between the primary particles of NCM811, leading to serious capacity fading.

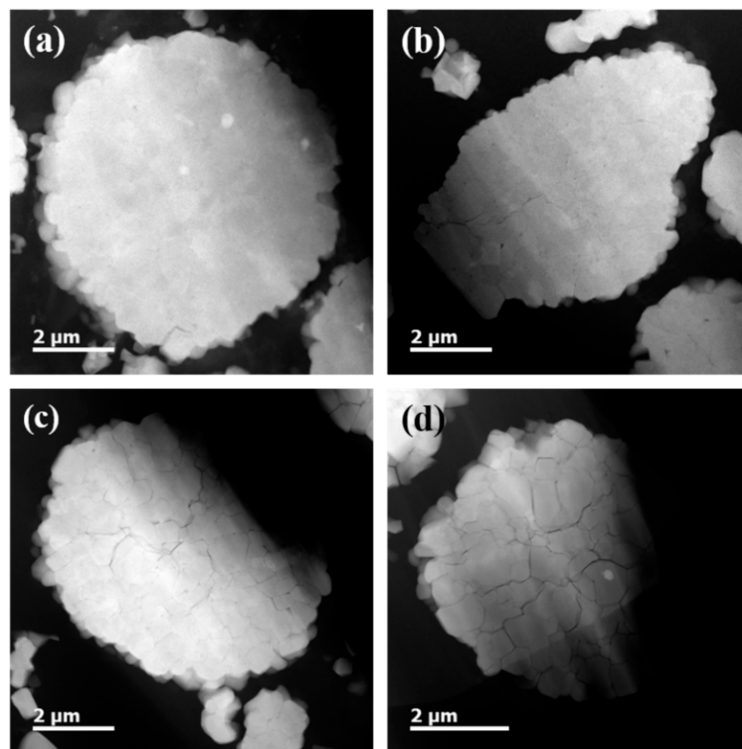


Figure 4. Cross-sectional STEM images of NCM811 after 50 cycles depending on the charging voltage: (a) before cycling at the open-circuit voltage (OCV), (b) 4.05 V, (c) 4.3 V, and (d) 4.5 V versus Li/Li⁺.

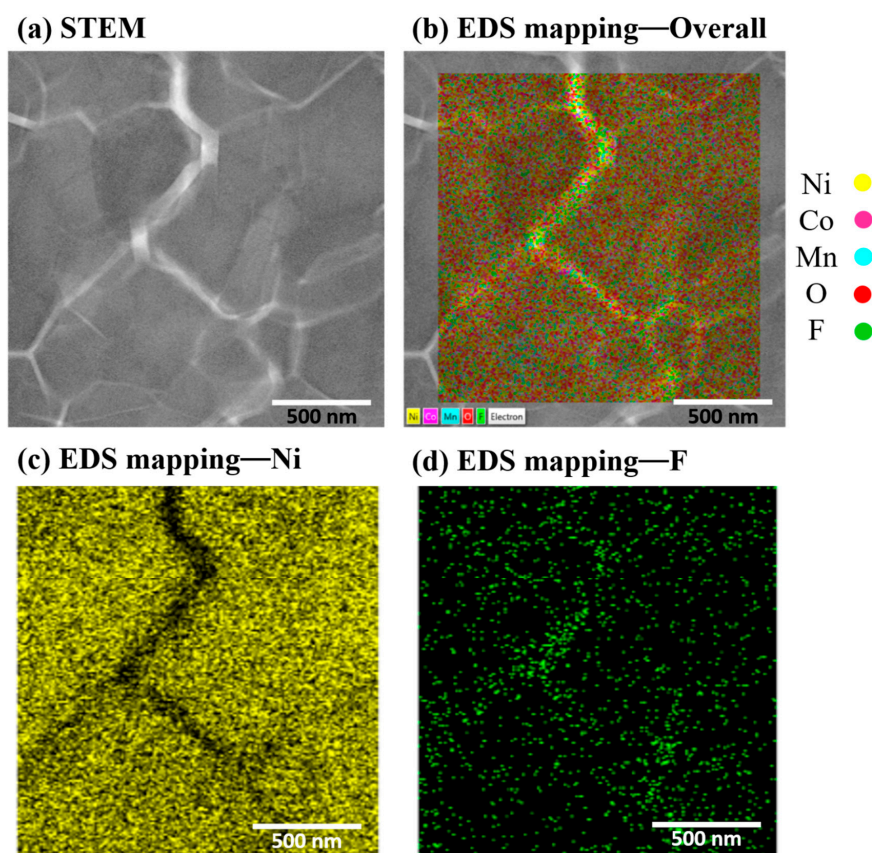


Figure 5. STEM images and the corresponding energy dispersive spectroscopy (EDS) mapping results for NCM811 after 600 cycles at 45 °C: (a) STEM image of the microcracks, and EDS mapping images of (b) overall, (c) Ni, and (d) F species.

Generally, transition metal dissolution from cathode materials can be confirmed by comparison of the contrast differences in the STEM images. In addition, it is possible to make a relative quantitative analysis of the transition metal dissolution by comparison of the degree of contrast because the ion beam is scattered from the prepared sample in dark-field STEM mode [40,41]. To clarify the effects of the exposure of the subsurface by microcrack propagation on the dissolution of transition metal from the cathode materials, the subsurface microcracks were analyzed by STEM. Figure 6 shows STEM images of the surface of the pristine primary particles and the surface formed by microcrack propagation. Compared with the surface of the pristine primary particles, the atomic column contrast was not uniform along the microcrack surface, indicating transition metal dissolution from the cycled NCM811. Figure 7 shows the brightness profile at the surface of the pristine primary particles and the microcracks based on the STEM observation. As expected, the contrast values obtained from the STEM analysis of the surface of the pristine primary particles are much more uniform, whereas the contrast values obtained from the newly formed surfaces by the microcrack propagation fluctuate significantly. Interestingly, such significant differences were obviously observed in the atomic column from the surface to ninth atomic inner layer. This result reveals that the transition metals in the cathode materials are dissolved into the electrolyte from the newly formed microcrack surface between the primary particles. Therefore, the electrolyte decomposition and transition metal dissolution on the surface formed by microcrack propagation between the primary particles is the main cause of NCM811 capacity fading.

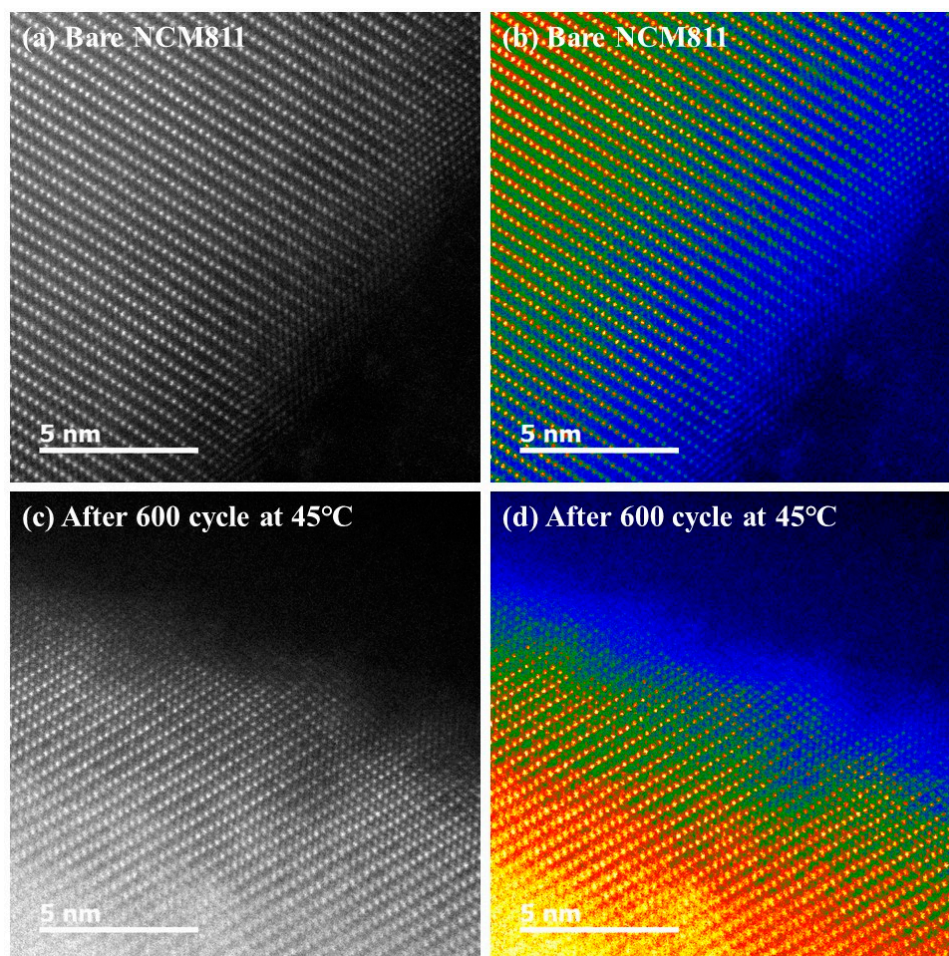


Figure 6. STEM images of the NCM811 surfaces: bare NCM811 (a,b) and after 600 cycles at 45 °C (c,d). (a) and (c) are the original STEM images, and (b) and (d) are converted from gray scale into color using Digital Micrograph.

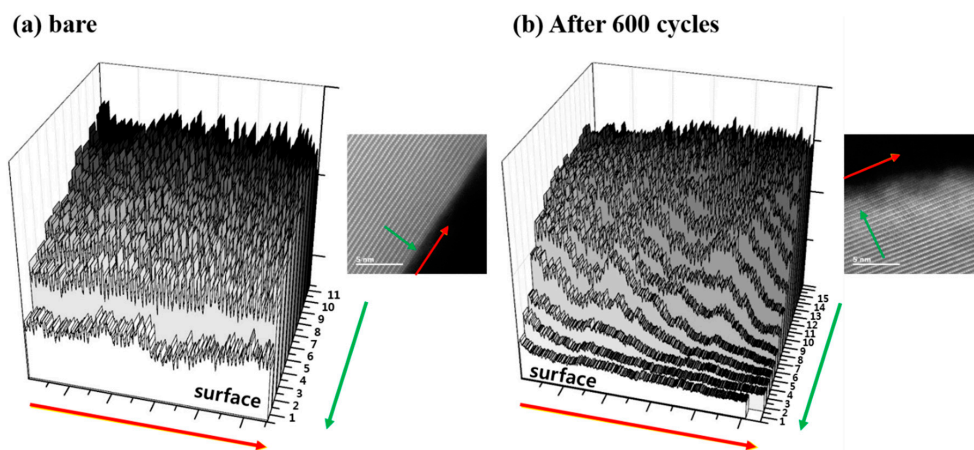


Figure 7. Brightness profile of the NCM811 STEM images: (a) bare and (b) after 600 cycles at 45 °C.

4. Conclusions

The factors affecting the capacity fading of the NCM811 cathode material were investigated. We found that there was a significant change in the *c*-axis length during charging and discharging, and this is one of the main causes of the formation and propagation of microcracks between the primary particles of NCM811. The formation and propagation of microcracks continuously produces new surfaces on the surface and interior of the NCM811 cathode material.

In addition, the electrolyte was decomposed on the microcrack surfaces, and the by-products from electrolyte decomposition form on this surface, leading to an increase in the impedance and resulting in poor electronic and ionic connectivity between the primary particles of NCM811. In addition, transition metals in the NCM811 cathode materials are dissolved into the electrolyte from the microcrack surfaces between primary particles. As a result, the electrolyte decomposition and transition metal dissolution on the newly formed surface are the main causes of NCM811 capacity fading.

We have shown that microcracks were formed between the primary particles during cycling, and the organic liquid electrolyte eventually penetrated and was decomposed at the newly formed surfaces of the primary particles. This side reaction resulted in an increase in the internal resistance and additional transition metal dissolution from the interior of the active material particles. In addition, we have demonstrated the main reason for the formation of microcracks was the change in the *c*-axis lattice parameter of NCM811 during de-lithiation, particularly the rapid change after the extraction of 0.5 Li⁺. These detrimental and complex effects have a significant influence on the electrochemical capability of NCM811. Consequently, to obtain better performance and a long battery life of Ni-rich NCM, the interparticle strength and structural stability must be improved.

Author Contributions: Conceptualization, Y.N.J., W.C., and J.-S.Y.; Methodology, Y.-k.A., Y.N.J., and W.C.; Software, W.C.; Validation, Y.-k.A., Y.N.J., K.J.K., and W.C.; Formal Analysis, Y.-k.A., Y.N.J., and W.C.; Investigation, J.-S.Y. and K.J.K.; Data Curation, Y.-k.A., Y.N.J., and W.C.; Writing-Original Draft Preparation, Y.-k.A., Y.N.J., and K.J.K.; Writing-Review & Editing, Y.-k.A., Y.N.J., W.C., and K.J.K.; Visualization, Y.-k.A., Y.N.J., and W.C.; Supervision, J.-S.Y. and K.J.K.; Project Administration, J.-S.Y. and K.J.K.; Funding Acquisition, J.-S.Y. and K.J.K.

Funding: This paper was supported by National Research Foundation of Korea grants (2018M1A2A2063354 and 2019R1A2C1004694). This work was also supported by a grant from the Fundamental R&D Program for Technology of World Premier Materials (10037919).

Conflicts of Interest: The authors declare no conflict of interest.

References

- Whittingham, M.S. Lithium batteries and cathode materials. *Chem. Rev.* **2004**, *104*, 4271–4302. [[CrossRef](#)] [[PubMed](#)]
- Liu, W.; Oh, P.; Liu, X.; Lee, M.-J.; Cho, W.; Chae, S.; Kim, Y.; Cho, J. Nickel-rich layered lithium transition-metal oxide for high-energy lithium-ion batteries. *Angew. Chem. Int. Ed.* **2015**, *54*, 4440–4457. [[CrossRef](#)]

3. Manthiram, A.; Knight, J.C.; Myung, S.-T.; Oh, S.-M.; Sun, Y.-K. Nickel-rich and lithium-rich layered oxide cathodes: Progress and perspectives. *Adv. Energy Mater.* **2016**, *6*, 1501010. [[CrossRef](#)]
4. Rozier, P.; Tarascon, J.M. Review-Li-rich layered oxide cathodes for next-generation Li-ion batteries: Chances and challenges. *J. Electrochem. Soc.* **2015**, *162*, A2490–A2499. [[CrossRef](#)]
5. Ahn, Y.-K.; Park, J.W.; Shin, D.W.; Cho, S.H.; Park, S.Y.; Kim, H.J.; Piao, Y.; Yoo, J.Y.; Kim, Y.S. Enhanced electrochemical capabilities of lithium ion batteries by structurally ideal AAO separator. *J. Mater. Chem. A* **2015**, *3*, 10715–10719. [[CrossRef](#)]
6. Noh, H.-J.; Youn, S.; Yoon, C.S.; Sun, Y.-K. Comparison of the structural and electrochemical properties of layered $\text{Li}[\text{Ni}_x\text{Co}_y\text{Mn}_z]\text{O}_2$ ($x = 1/3, 0.5, 0.6, 0.7, 0.8$ and 0.85) cathode material for lithium-ion batteries. *J. Power Sources* **2013**, *233*, 121–130. [[CrossRef](#)]
7. Schipper, F.; Erickson, E.M.; Erk, C.; Shin, J.-Y.; Chesneau, F.F.; Aurbach, D. Review-recent advances and remaining challenges for lithium ion battery cathodes: I. nickel-rich, $\text{LiNi}_x\text{Co}_y\text{Mn}_z\text{O}_2$. *J. Electrochem. Soc.* **2017**, *164*, A6220–A6228. [[CrossRef](#)]
8. Kojima, T.; Ishizu, T.; Horiba, T.; Yoshikawa, M. Development of lithium-ion battery for fuel cell hybrid electric vehicle application. *J. Power Sources* **2009**, *189*, 859–863. [[CrossRef](#)]
9. Darcovich, K.; Henquin, E.R.; Kenney, B.; Davidson, I.J.; Saldanha, N.; Beausoleil-Morrison, I. Higher-capacity lithium ion battery chemistries for improved residential energy storage with micro-cogeneration. *Appl. Energy* **2013**, *111*, 853–861. [[CrossRef](#)]
10. Sun, Y.K.; Kang, H.B.; Myung, S.T.; Prakash, J. Effect of manganese content on the electrochemical and thermal stabilities of $\text{Li}[\text{Ni}_{0.58}\text{Co}_{0.28-x}\text{Mn}_{0.14+x}]\text{O}_2$ cathode materials for lithium-ion batteries. *J. Electrochem. Soc.* **2010**, *157*, A1335–A1340. [[CrossRef](#)]
11. Lee, B.R.; Noh, H.J.; Myung, S.T.; Amine, K.; Sun, Y.K. High-voltage performance of $\text{Li}[\text{Ni}_{0.55}\text{Co}_{0.15}\text{Mn}_{0.30}]\text{O}_2$ positive electrode material for rechargeable Li-ion batteries. *J. Electrochem. Soc.* **2011**, *158*, A180–A186. [[CrossRef](#)]
12. Manthiram, A.; Song, B.; Li, W. A perspective on nickel-rich layered oxide cathodes for lithium-ion batteries. *Energy Storage Mater.* **2017**, *6*, 125–139. [[CrossRef](#)]
13. Eom, J.; Kim, M.G.; Cho, J. Storage characteristics of $\text{LiNi}_{0.8}\text{Co}_{0.1+x}\text{Mn}_{0.1-x}\text{O}_2$ ($x=0, 0.03,$ and 0.06) cathode materials for lithium batteries. *J. Electrochem. Soc.* **2008**, *155*, A239–A245. [[CrossRef](#)]
14. Li, X.; Zhang, K.; Wang, M.; Liu, Y.; Qu, M.; Zhao, W.; Zheng, J. Dual functions of zirconium modification on improving the electrochemical performance of Ni-rich $\text{LiNi}_{0.8}\text{Co}_{0.1}\text{Mn}_{0.1}\text{O}_2$. *Sustain Energy Fuel.* **2018**, *4*, 413–421. [[CrossRef](#)]
15. Liu, S.; Xiong, L.; He, C. Long cycle life lithium ion battery with lithium nickel cobalt manganese oxide (NCM) cathode. *J. Power Sources* **2014**, *261*, 285–291. [[CrossRef](#)]
16. Song, H.J.; Jang, S.H.; Ahn, J.; Oh, S.H.; Yim, T. Artificial cathode-electrolyte interphases on nickel-rich cathode materials modified by silyl functional group. *J. Power Sources* **2019**, *416*, 1–8. [[CrossRef](#)]
17. Kim, K.M.; Ly, N.V.; Won, J.H.; Lee, Y.G.; Cho, W.I.; Ko, J.M.; Kaner, R.B. Improvement of lithium-ion battery performance at low temperature by adopting polydimethylsiloxane-based electrolyte additives. *Electrochim. Acta* **2014**, *136*, 182–188. [[CrossRef](#)]
18. Li, B.; Xu, M.; Li, T.; Li, W.; Hu, S. Prop-1-ene-1, 3-sultone as SEI formation additive in propylene carbonate-based electrolyte for lithium ion batteries. *Electrochem. Commun.* **2012**, *17*, 92–95. [[CrossRef](#)]
19. Kim, H.; Kim, M.G.; Jeong, H.Y.; Nam, H.; Cho, J. A new coating method for alleviating surface degradation of $\text{LiNi}_{0.6}\text{Co}_{0.2}\text{Mn}_{0.2}\text{O}_2$ cathode material: Nanoscale surface treatment of primary particles. *Nano Lett.* **2015**, *15*, 2111–2119. [[CrossRef](#)]
20. Schipper, F.; Bouzaglo, H.; Dixit, M.; Erickson, E.M.; Weigel, T.; Talianker, M.; Grinblat, J.; Burstein, L.; Schmidt, M.; Lampert, J.; et al. From Surface ZrO_2 coating to bulk Zr doping by high temperature annealing of nickel-rich lithiated oxides and their enhanced electrochemical performance in lithium ion batteries. *Adv. Energy Mater.* **2018**, *8*, 1701682. [[CrossRef](#)]
21. Park, K.J.; Choi, M.J.; Maglia, F.; Kim, S.J.; Kim, K.H.; Yoon, C.S.; Sun, Y.K. High-capacity concentration gradient $\text{Li}[\text{Ni}_{0.865}\text{Co}_{0.120}\text{Al}_{0.015}]\text{O}_2$ cathode for lithium-ion batteries. *Adv. Energy Mater.* **2018**, *8*, 1703612. [[CrossRef](#)]
22. Sun, H.H.; Manthiram, A. Impact of microcrack generation and surface degradation on a nickel-rich layered $\text{Li}[\text{Ni}_{0.9}\text{Co}_{0.05}\text{Mn}_{0.05}]\text{O}_2$ cathode for lithium-ion batteries. *Chem. Mater.* **2017**, *29*, 8486–8493. [[CrossRef](#)]

23. Lim, J.M.; Hwang, T.; Kim, D.; Park, M.S.; Cho, K.; Cho, M. Intrinsic origins of crack generation in Ni-rich $\text{LiNi}_{0.8}\text{Co}_{0.1}\text{Mn}_{0.1}\text{O}_2$ layered oxide cathode material. *Sci. Rep.* **2017**, *7*, 39669. [[CrossRef](#)] [[PubMed](#)]
24. Zheng, S.; Huang, R.; Makimura, Y.; Ukyo, Y.; Fisher, C.A.; Hirayama, T.; Ikuhara, Y. Microstructural changes in $\text{LiNi}_{0.8}\text{Co}_{0.15}\text{Al}_{0.05}\text{O}_2$ positive electrode material during the first cycle. *J. Electrochem. Soc.* **2011**, *158*, A357–A362. [[CrossRef](#)]
25. Miller, D.J.; Proff, C.; Wen, J.G.; Abraham, D.P.; Bareño, J. Observation of microstructural evolution in Li battery cathode oxide particles by in situ electron microscopy. *Adv. Energy Mater.* **2013**, *3*, 1098–1103. [[CrossRef](#)]
26. Kang, K.S.; Choi, S.; Song, J.H.; Woo, S.G.; Jo, Y.N.; Chow, J.; Yim, T.; Yu, J.S.; Kim, Y. Effect of additives on electrochemical performance of lithium nickel cobalt manganese oxide at high temperature. *J. Power Sources* **2014**, *253*, 48–54. [[CrossRef](#)]
27. Liu, T.; Garsuch, A.; Chesneau, F.; Lucht, B.L. Surface phenomena of high energy $\text{Li}(\text{Ni}_{1/3}\text{Co}_{1/3}\text{Mn}_{1/3})\text{O}_2$ /graphite cells at high temperature and high cutoff voltages. *J. Power Sources* **2014**, *269*, 920–926. [[CrossRef](#)]
28. Chen, H.; Hu, Q.; Huang, Z.; He, Z.; Wang, Z.; Guo, H.; Li, X. Synthesis and electrochemical study of Zr-doped $\text{Li}[\text{Li}_{0.2}\text{Mn}_{0.54}\text{Ni}_{0.13}\text{Co}_{0.13}]\text{O}_2$ as cathode material for Li-ion battery. *Ceram. Int.* **2016**, *42*, 263–269. [[CrossRef](#)]
29. Xi, Y.; Liu, Y.; Zhang, D.; Jin, S.; Zhang, R.; Jin, M. Comparative study of the electrochemical performance of $\text{LiNi}_{0.5}\text{Co}_{0.2}\text{Mn}_{0.3}\text{O}_2$ and $\text{LiNi}_{0.8}\text{Co}_{0.1}\text{Mn}_{0.1}\text{O}_2$ cathode materials for lithium ion batteries. *Solid State Ion.* **2018**, *327*, 27–31. [[CrossRef](#)]
30. Lu, Z.; Beaulieu, L.Y.; Donaberger, R.A.; Thomas, C.L.; Dahn, J.R. Synthesis, structure, and electrochemical behavior of $\text{Li}[\text{Ni}_x\text{Li}_{1/3-2x/3}\text{Mn}_{2/3-x/3}]\text{O}_2$. *J. Electrochem. Soc.* **2002**, *149*, A778–A791. [[CrossRef](#)]
31. Zhang, Z.; Chen, D.; Chang, C. Improved electrochemical performance of $\text{LiNi}_{0.8}\text{Co}_{0.1}\text{Mn}_{0.1}\text{O}_2$ cathode materials via incorporation of rubidium cations into the original Li sites. *RSC Adv.* **2017**, *7*, 51721–51728. [[CrossRef](#)]
32. Wang, M.; Zhang, R.; Gong, Y.; Su, Y.; Xiang, D.; Chen, L.; Chen, Y.; Luo, M.; Chu, M. Improved electrochemical performance of the $\text{LiNi}_{0.8}\text{Co}_{0.1}\text{Mn}_{0.1}\text{O}_2$ material with lithium-ion conductor coating for lithium-ion batteries. *Solid State Ion.* **2017**, *312*, 53–60. [[CrossRef](#)]
33. Kim, U.H.; Lee, E.J.; Yoon, C.S.; Myung, S.T.; Sun, Y.K. Compositionally graded cathode material with long-term cycling stability for electric vehicles application. *Adv. Energy Mater.* **2016**, *6*, 1601417. [[CrossRef](#)]
34. Kondrakov, A.O.; Schmidt, A.; Xu, J.; Geßwein, H.; Mönig, R.; Hartmann, P.; Sommer, H.; Brezesinski, T.; Janek, J. Anisotropic lattice strain and mechanical degradation of high- and low-nickel NCM cathode materials for Li-ion batteries. *J. Phys. Chem. C* **2017**, *121*, 3286–3294. [[CrossRef](#)]
35. Ryu, H.H.; Park, K.J.; Yoon, C.S.; Sun, Y.K. Capacity fading of Ni-rich $\text{Li}[\text{Ni}_x\text{Co}_y\text{Mn}_{1-x-y}]\text{O}_2$ ($0.6 \leq x \leq 0.95$) cathodes for high-energy-density lithium-ion batteries: Bulk or surface degradation? *Chem. Mater.* **2018**, *30*, 1155–1163. [[CrossRef](#)]
36. Kim, J.H.; Woo, S.C.; Park, M.S.; Kim, K.J.; Yim, T.; Kim, J.S.; Kim, Y.J. Capacity fading mechanism of LiFePO_4 -based lithium secondary batteries for stationary energy storage. *J. Power Sources* **2013**, *229*, 190–197. [[CrossRef](#)]
37. Woo, S.G.; Kim, J.H.; Kim, H.R.; Cho, W.; Yu, J.S. Failure mechanism analysis of $\text{LiNi}_{0.88}\text{Co}_{0.09}\text{Mn}_{0.03}\text{O}_2$ cathodes in Li-ion full cells. *J. Electroanal. Chem.* **2017**, *799*, 315–320. [[CrossRef](#)]
38. Li, J.; Downie, L.E.; Ma, L.; Qiu, W.; Dahn, J.R. Study of the failure mechanisms of $\text{LiNi}_{0.8}\text{Mn}_{0.1}\text{Co}_{0.1}\text{O}_2$ cathode material for lithium ion batteries. *J. Electrochem. Soc.* **2015**, *162*, A1401–A1408. [[CrossRef](#)]
39. Kim, H.R.; Woo, S.G.; Kim, J.H.; Cho, W.; Kim, Y.J. Capacity fading behavior of Ni-rich layered cathode materials in Li-ion full cells. *J. Electroanal. Chem.* **2016**, *782*, 168–173. [[CrossRef](#)]
40. LeBeau, J.M.; Findlay, S.D.; Allen, L.J.; Stemmer, S. Standardless atom counting in scanning transmission electron microscopy. *Nano Lett.* **2010**, *10*, 4405–4408. [[CrossRef](#)] [[PubMed](#)]
41. Lee, S.; Oshima, Y.; Sawada, H.; Hosokawa, F.; Okunishi, E.; Kaneyama, T.; Kondo, Y.; Takagi, H.; Tanishiro, Y.; Takayanagi, K. Counting lithium ions in the diffusion channel of an LiV_2O_4 crystal. *J. Appl. Phys.* **2011**, *109*, 113530. [[CrossRef](#)]

